ADVANCING EARTH AND SPACE SCIENCE

# Geophysical Research Letters

RESEARCH LETTER
10.1029/2022GL100622

**Key Points:**

- We present novel high-resolution airborne observations of the kinematics of shoaling and breaking internal waves
- We find that the active breaking regions of the internal wave drive strong convergence/divergence
- The spatial variability of the internal wave is shown to occur over a broad range of scales, from a few to a few hundred meters

**Correspondence to:**
T. Vrećica and L. Lenain,
vrecica@gmail.com;
llenain@ucsd.edu

**Citation:**
Vrećica, T., Pizzo, N., & Lenain, L. (2022). Airborne observations of shoaling and breaking internal waves. *Geophysical Research Letters*, *49*, e2022GL100622. https://doi.org/10.1029/2022GL100622

Received 19 AUG 2022
Accepted 2 NOV 2022



# Airborne Observations of Shoaling and Breaking Internal Waves

**Teodor Vrećica[1,2], Nick Pizzo[1], and Luc Lenain[1]**

[1]Scripps Institution of Oceanography, University of California San Diego, San Diego, CA, USA, [2]Mathematical Institute of the Serbian Academy of Sciences and Arts, Belgrade, Serbia

## Abstract

Internal waves (IW) are crucial contributors to the transport of sediment, heat, and nutrients in coastal areas. While IW have been extensively studied using point measurements, their spatial variability is less well understood. In this paper we present a unique set of high-resolution infrared imagery collected from a helicopter, hovering over very energetic shoaling and breaking IW. We compute surface velocities by tracking the evolution of thermal structures at the ocean surface and find horizontal velocity gradients with magnitudes that are more than 100 times the Coriolis frequency. Under the assumption of no vertical shear we determine vertical velocities from the obtained horizontal divergence estimates and identify areas of the wave undergoing breaking. The spatial variability of the internal wave occurs on scales from a few to a few hundred meters. These results highlight the need to collect spatio-temporal observations of the evolution of IW in coastal areas.

## Plain Language Summary

Oceanic internal waves (IW) form between heavier and lighter ocean water in the ocean interior, covering a wide range of temporal and spatial scales. They are amongst some of the key processes in the ocean—they facilitate transport of heat, sediment, and nutrients which have important implications for plankton and other ocean lifeforms, and serve as a pathway of energy from large to small scale flows. Yet, they are often measured using a point based approach (e.g., a buoy), which is unable to provide a full picture of the spatial variability of these waves and hence might not capture crucial behavior. Here, a unique set of high resolution airborne measurements is presented, covering several kilometers of a shoaling (and breaking) internal wave packet. Velocities at the sea surface are determined from infrared video imagery, using the temperature of the water as a tracer. By applying simple models to the velocity data (no change of horizontal velocity with depth), we show that variations in the vertical transport and in breaking characteristics are significant on many different spatial scales. This work is a step forward in understanding and quantifying the spatial variability of IW and processes associated with their breaking induced flow.

## 1. Introduction

Internal waves occur at a density interface, and in deep-water may be generated through tidal or wind forcing (Alford, 2001; Baines, 1982; Helfrich & Melville, 2006). Alternatively, they can be locally generated on the continental shelf (e.g., Sandstrom & Elliott, 1984; Shroyer et al., 2010). No matter the generation mechanism or location, internal waves (IW) on the inner-shelf can shoal and break, modulating the transport of sediment, heat, contaminants, and nutrients (e.g., Lamb, 2014; Sinnett et al., 2022). They are crucial for understanding the rates of energy dissipation and mixing (Jones et al., 2020; Moum et al., 2007). One of their most important characteristics is their large vertical velocities (in comparison to typical upwelling indices, Bakun, 1973), which facilitates vertical transport of suspended material, heat and horizontal momentum.

Traditional methods for measuring IW include in-situ moorings and towed instruments (Colosi et al., 2018; Moum et al., 2002). By employing ADCPs and temperature sensors on fixed or freely drifting moorings, it is possible to determine velocities and density as a function of depth. The energy dissipation rate can subsequently be determined from these measurements (e.g., Moum et al., 2007). While a mooring yields high resolution temporal information at one location, it does not capture the directionality and scales of the horizontal spatial variability of an internal wave, particularly as it shoals and breaks. Several previous studies have used a spatial array of moorings to try to address this shortcoming (Badiey et al., 2013; J. Thomas et al., 2016; McSweeney, Lerczak, Barth, Becherer, MacKinnon, et al., 2020), but even these do not capture the fine scale three dimensional structures characteristic of an internal wave (Lenain & Pizzo, 2021; Woods, 1968). Most theoretical studies of internal wave propagation are restricted to two dimensional waves, although some studies (e.g., Pullin &

Grimshaw, 1985; Venayagamoorthy & Fringer, 2006, 2007; Vlasenko & Stashchuk, 2007) predict the generation of lateral instabilities for steep waves, together with the fully turbulent and three dimensional internal wave breaking process, hinting at the limitation of two dimensional approaches to describing processes that are fundamentally three dimensional.

Spatio-temporal evolution of an internal wave can be inferred through remote sensing approaches, such as synthetic-aperture radar (SAR, e.g., see Romeiser & Graber, 2015) or X-band radars (e.g., Celona et al., 2021; Haney et al., 2021). These indirect observational techniques rely on the modulation of surface roughness due to wave-current interaction (Alpers, 1985; Craig et al., 2012) to infer the propagation speed and currents induced by the internal wave. Direct observations of the modulation of surface gravity wave spectra by internal wave currents are presented in Lenain and Pizzo (2021). They found significant spatial variability in the surface signature of sea surface temperature (see Figure 3 of Lenain & Pizzo, 2021) potentially associated with transverse instabilities. Similar transverse structures were also recently observed using a fiber optic distributed temperature sensing seafloor array off La Jolla, CA (Lucas & Pinkel, 2022). However, none of these approaches can quantify the spatio-temporal evolution of the IW, as they do not provide direct spatial observations of the kinematics during steepening and breaking. Crucially, the velocity field and its gradients is often not measured, therefore limiting our ability to develop better physical understanding of these processes, including their vertical and horizontal transport.

In this work, we present novel observations of the surface properties of shoaling and breaking IW, collected from the Modular Aerial Sensing System (MASS, Melville et al., 2016) installed on a helicopter. By slowly moving in the transverse direction (i.e., parallel to the wave front) of the IW, we obtained high-resolution (O(1) m) observations of the spatio-temporal evolution of surface velocities and shoaling and breaking properties.

This paper is structured as follows: the overview of the experiment and processing techniques is given in Section 2 while spectral analysis of the transverse structures found in the sea surface temperature near the IW is presented in Section 3.2. In Sections 3.3 and 3.4, analysis of surface kinematics computed from the infrared camera is discussed, with emphasis on vertical velocities inferred from horizontal divergence, and the derivation of a simple criteria to determine areas where the IW are actively breaking is presented. Conclusions are given in Section 4.

## 2. Field Experiment and Methods

### 2.1. Field Campaign

The observations presented here were collected near Point Sal, California as part of the Inner-Shelf Dynamics Experiment (ISDE, Kumar et al., 2021) pilot program in August 2015. The primary objective of this project was to investigate and observe the role of surface and internal wave processes on the dynamics, transport, currents and mixing in the inner-shelf. In this part of the project, we investigated the use of an instrumented helicopter (Bell 206L-III Long Ranger operated by Aspen Helicopter, Oxnard, CA, shown in Figure 1) to enable prolonged observations of specific portions of the sea surface (as opposed to a fixed-wing aircraft) by hovering at approximately the same location for several minutes. One of the surveys on 1 August 2015 was focused on an internal wave shoaling approximately 1 km SW of Point Sal, CA. Handheld DSLR photos of the IW are shown in Figure 1, clearly exhibiting alternating bands of smooth and rough surfaces induced by the currents associated with an IW, as well as the convergence of foam (surfactants). Also evident is the severe modulation of ocean color over very short length scales (O(1) m) hinting at the strong mixing and vertical transport across the full water column (ranging from 20 to 25 m depth at this location) as the IW propagates toward shore.

The helicopter used in the experiment was instrumented with the MASS, developed at the Air-Sea Interaction Laboratory, Scripps Institution of Oceanography (see Melville et al., 2016; Lenain & Melville, 2017, for details). Here, we focus on the analysis of the sea surface temperature imagery collected from a FLIR SC6000 QWIP camera (14-bit, 640 × 512 pixel resolution output at 50 Hz). A Novatel LN200 tactical-grade inertial measurement unit (IMU) is used to georeference each infrared image into the earth-coordinate frame. This IMU contains closed-loop fiber optic gyros and solid-state silicon accelerometers with 200-Hz data output rates and is coupled with a Novatel PwrPak7 dual-antenna GPS receiver. For this flight, the highest spatial resolution we could obtain per individual georeferenced image, based on the instrument altitude, was approximately 0.4 m. In addition, sea surface temperature (Figure 2) maps were produced from these infrared images by conditionally averaging all data available, per location, to improve the signal-to-noise ratio. An overview of the observed IW and the

10.1029/2022GL100622


**Figure 1.** Handheld photographs of the sea surface taken from the helicopter at 23:15 UTC 01 August 2015, flying at elevations of 250–300 m above the internal wave considered in this analysis. The helicopter used in this field campaign, a Bell 206-LIII Long-Range operated by Aspen Helicopter in Oxnard, CA is also shown. Note the convergence of foam at the leading edge of the IW packet, and the cross-wave structure of the packet outlined by a change in water color.

surrounding area is given in Figure 2. The bathymetry (together with a satellite image of land area) is shown in Figure 2a. The bathymetry south of Point Sal is initially steep (from the coastline up to 15 m depth), after which the slope becomes much milder. The water depth is on average approximately 25 m in the area where the IW is observed. The helicopter passed over the internal wave at a speed ranging from approximately 2 to 8 m/s, so that in turn there was approximately up to 50 s of observations for each surveyed location, while it remained at the initial area of observation for approximately 3 min.

### 2.2. Computing Surface Velocities From Infrared Imagery

The thermal structures present in each georeferenced image is sufficient to perform cross-correlation analysis similar to that of Particle Image Velocimetry (PIV), on successive surface infrared images. Each of the PIV images were produced from georeferenced infrared images collected at 50 Hz and then conditionally averaged (for 1 s) to improve the signal-to-noise ratio. This leads to 50 frames contributing to each pixel of the PIV image under consideration. Here we use an adaptive PIV algorithm developed by Fabrice Veron's group at University of Delaware (M. Thomas et al., 2005; Buckley & Veron, 2017). This algorithm relies on a pyramid cascade of increasingly smaller and shifting interrogation windows to achieve large dynamical range in the detected velocity. A central difference scheme is used to compute displacements within the images. Note, here gradients of SST images are used. Pairs of images were processed with a final interrogation window of $8 \times 8$ pixels, with 50% window overlap, leading to a velocity vector measurement on a 2D surface grid with 8 m spacing in each direction. A time difference between images $dt$ of 20 s was used in the analysis. All velocity vectors with normalized correlation lower than 0.5 were discarded. The obtained velocity maps are then conditionally averaged over the total amount of data collected for each grid point (up to 50 s). Convergence of the obtained PIV velocity products, with respect to the time step ($dt$) and the interrogation window size, was carefully validated.

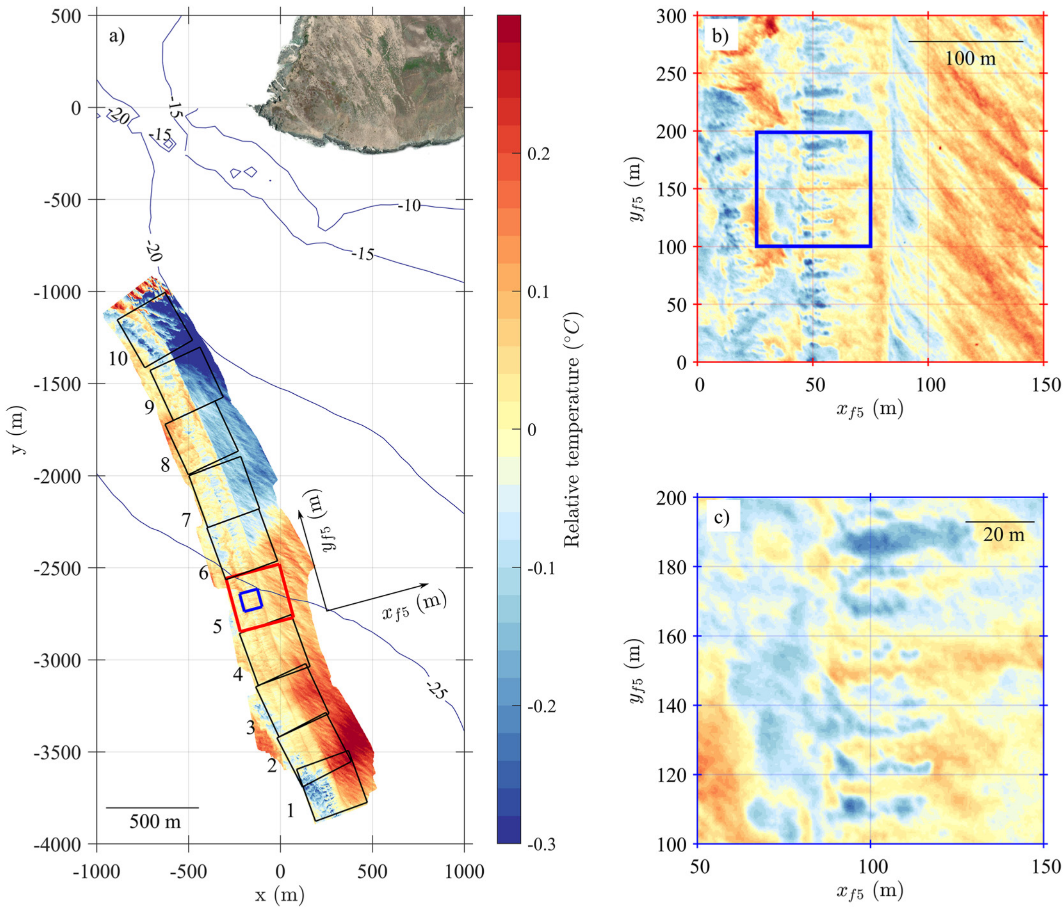


**Figure 2.** Sea surface map showing the relative surface temperature (surface temperature minus the mean temperature in the observed area) of a shoaling internal wave, as observed from the MASS infrared camera. (a) An overview of the area, with Point Sal, CA (chosen as origin of the coordinate system) to the northeast of the internal wave. The black rectangles indicate 300 by 300 m$^2$ areas for which the analysis is performed. (b and c) shows a zoomed-in version of Section 5, highlighting the fine scale transverse structures in the wake of the leading edge of the internal wave packet.

The vertical velocity $w$ is estimated from the continuity equation, $\nabla \cdot \mathbf{u} = 0$. Here $u$ is the velocity in the direction of the propagating IW, while $v$ is in the direction normal to this, in a right handed coordinate system, in the horizontal plane. We depth integrate the continuity equation to find

$$w(0) = -\int_{-H}^{0} \left( \frac{\partial u}{\partial x} + \frac{\partial v}{\partial y} \right) dz = -H \left( \frac{1}{H} \frac{\partial}{\partial x} \int_{-H}^{0} u dz + \frac{1}{H} \frac{\partial}{\partial y} \int_{-H}^{0} v dz \right) \tag{1}$$

$$= -H \left( U_x + V_y \right), \tag{2}$$

where we define

$$U \equiv \frac{1}{H} \int_{-H}^{0} u dz; V \equiv \frac{1}{H} \int_{-H}^{0} v dz. \tag{3}$$

Our lack of subsurface velocity measurements does not allow us to perform these vertical integrations, so as a first approximation, motivated by the visible imagery shown in Figure 1 which displays sediment transport at the surface, we assume that the horizontal velocities are depth uniform, that is, $U = u$, $V = v$, allowing us to estimate these integrals from surface measurements.

Next, the propagation speed of the IW packet is estimated using collocated SST images from two MASS overflights (Figure 2) and a second overflight conducted at higher altitude approximately to 30 min later by tracking the position of the thermal surface signature of the IW packet over this temporal interval. We found a propagation speed $c$ of approximately 0.13 m/s (along wave average) toward the east.

## 3. Results

### 3.1. Sea Surface Temperature

Figure 2a shows strong modulations of the SST associated with the passing IW, extending transversely over more than 3 km. Notice the horseshoe like patterns in the wake of the IW. The middle portion of the IW, around $y = 2$–$3$ km, exhibits a wave train like structure that abruptly collapses further north, while stronger modulations of the SST can still be seen to the south. We also find a wealth of thermal structures at much smaller scales associated with the passing IW. This is illustrated in Figures 2b and 2c, where rotated images of area 5 (highlighted in Figure 2a) at increasingly smaller scales show the presence of transverse (along $y_f$ axes) quasi-periodic structures within the IW, with length scales of approximately 10–30 m. These structures are reminiscent of *breaking surface gravity waves*, where formation of such streaks have been observed in thermal imagery of the ocean surface (e.g., Handler et al., 2012; Huang et al., 2012) and hint at the route from the approximately two dimensional IW to fully three dimensional turbulent dissipation process. The scales of these structures might also be useful in estimating the energy dissipated by these shoaling and breaking events, following a similar approach in the surface waves community from Drazen et al. (2008). However, this falls outside of the scope of the current manuscript and is not pursued in more detail here.

### 3.2. Transverse Structures

To characterize the spatial variability of the transverse (along $y_f$ axes) structures observed in the sea surface temperature imagery, the sampled region is divided into 10 sections, as indicated in Figure 2a. These areas are 300 by 300 m$^2$, rotated to be oriented with the leading edge of the IW packet, located at $x_{fn} = 0$ m, where $n$ is the index of the section number. A SST map of each area is presented in Figure 3. Note the presence of transverse structures between waves, with wavelengths in the range of 25–40 m.

The evolution of the wavenumber spectrum of the along-wave sea surface temperature, as a function of cross-wave distance $x_{fn}$, is shown in Figures 4a and 4c for two sections (1 and 5). We find that the IW strongly modulates the thermal structure of the ocean surface as it propagates toward shore, modulating spectral levels for wavenumbers $k$ smaller than 3 rad/m by up to a factor 10.

In each one of these cases, the thermal surface signatures of the leading edge of the IW packet is followed (downstream, $x_f < 0$) by a relatively smooth band, then a series of streaks, manifesting as alternating patches of colder and warmer water at the surface, hinting at the intense vertical transport and mixing occurring at these scales. These patches appear at 25 (Figure 4b) to 50 (Figure 4d) meters from the leading edge of the IW train. They cover a relatively wide range of wavelengths, from 3 to 100 m. The total variance of sea surface temperature is shown to dramatically increase (as indicated in the subplots of Figures 4a and 4c) downstream of the smooth band preceding the leading edge of the IW packet, again hinting at significant mixing and vertical transport (e.g., colder deeper water advected up to the surface) at smaller scales.

### 3.3. Surface Kinematics

Maps of surface velocities $u$ and $v$ computed from PIV along with sea surface temperature are shown in Figures 5a–5c. The cross-wave velocities (Figure 5b) show a clear periodic pattern (up to $y = -1400$ m), while the areas outside of the waves have an ambient current in an opposing direction to the direction of propagation of the IW. A significant reduction in current magnitude occurs at approximately $y = -3000$ m. Much less structure is apparent in $v$ (Figure 5c). Surface components of strain rate ($\psi = \partial v/\partial x + \partial u/\partial y$), divergence ($\nabla = \partial u/\partial x + \partial v/\partial y$), and vorticity ($\omega = \partial v/\partial x - \partial u/\partial y$), normalized by the Coriolis frequency ($f$), are shown in Figures 5d–5f. We find the strain rate to be significantly modulated by the passing IW, exceeding $100f$ near the leading edge of the IW packet, and clearly showing the transverse periodic structure discussed above. Similarly, a strong line of convergence (larger than $100f$!), which by continuity implies a strong localized downwelling current, can be seen at the front of the wave (Figure 5e) where the normalized divergence is shown, followed by alternating regions of divergence and convergence. There is little apparent structure in the plot of surface vorticity (Figure 5f), however

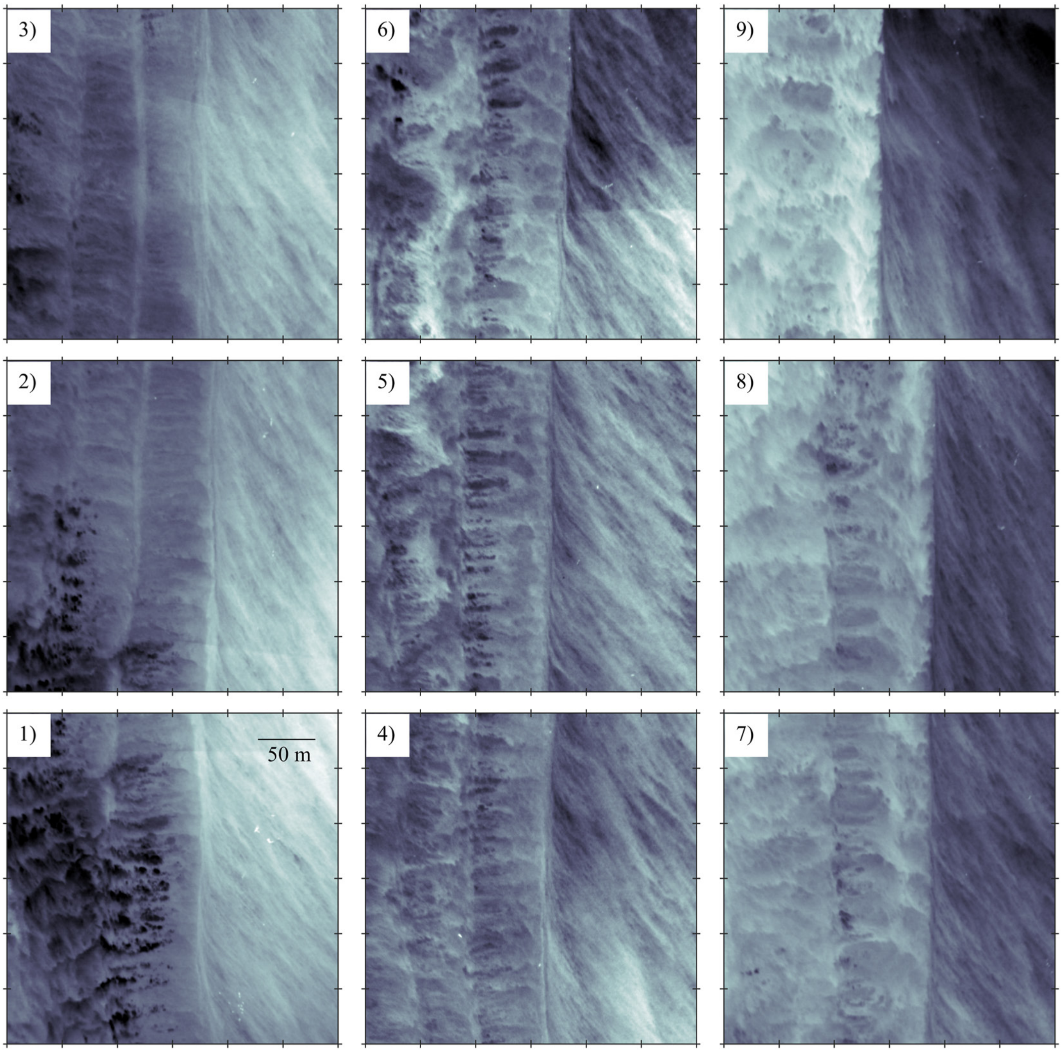


**Figure 3.** Evolution of the thermal surface signature along the internal wave packet (Section 1 through 9 highlighted in Figure 2). Notice the range of spatial scales present, particularly in the transverse direction. Horseshoe like patterns in the wake of the internal wave front are evident in nearly all of the panels. These structures provide a pathway from the initially quasi-two-dimensional linear internal wave to three dimensional dissipative events. Dark color is colder, while brighter colors correspond to warmer temperatures.

it should be kept in mind that the dissipation regime occurs on scales which are far smaller than the horizontal resolution of the obtained velocity field ($dx = 8$ m), see Gregg (1989) for more details.

### 3.4. Vertical Transport and Internal Wave Breaking Criteria

Here we utilize a kinematic wave breaking criteria to characterize the breaking state of the internal wave (Orlanski & Bryan, 1969). It assumes that a region of a shoaling internal wave is breaking if the surface velocity in the direction of the internal wave propagation (minus the ambient current) is larger than that of the propagation speed $c$ of the internal wave such that

$$\mathcal{U}/c - 1 > 0, \tag{4}$$

where $\mathcal{U}$ is the cross-wave surface velocity minus the ambient current (defined as the surface velocity outside of the IW area), and $c$ is speed of propagation of the internal wave, which was determined as a function of the along wave distance.

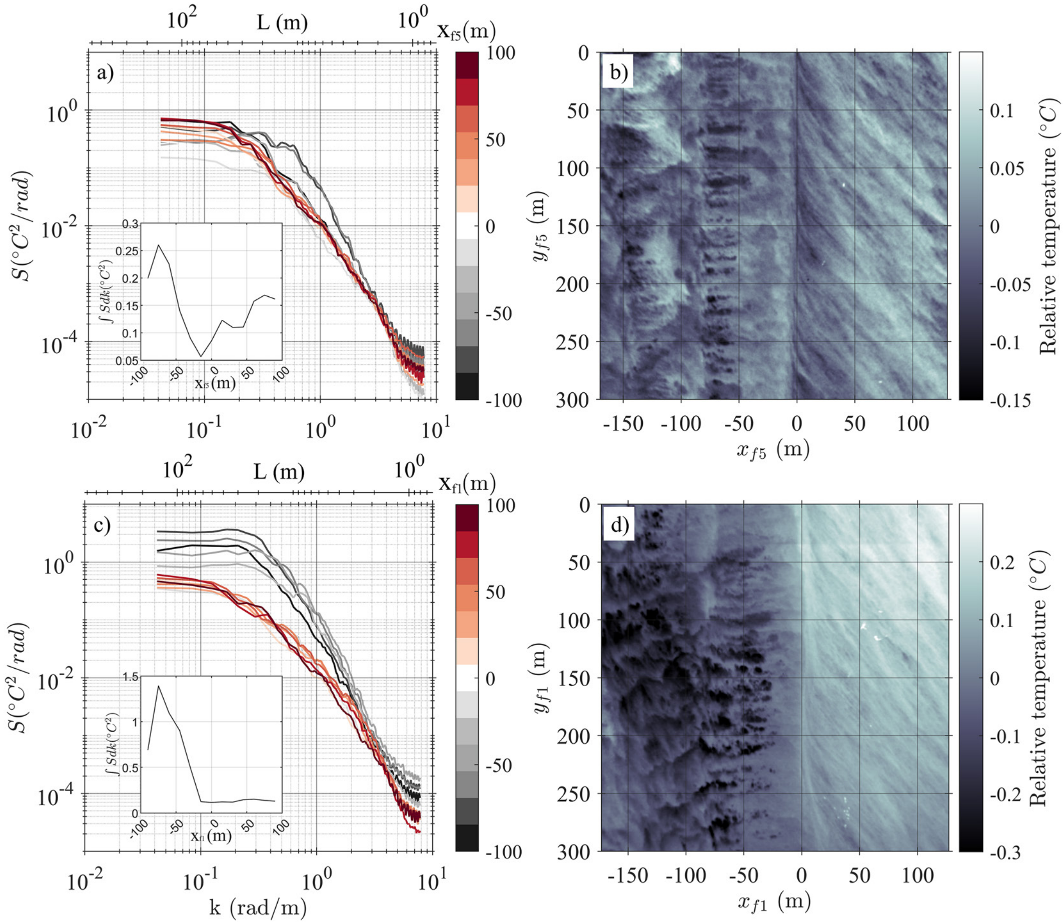

**Figure 4.** Comparison of wave spectral properties for two different areas (1 and 5, as shown in Figure 2). (a and c) Spectra of alongwave temperature variation (averaged over 15 m in the crosswave direction) for the two areas, as a function of distance from the leading edge of the IW packet $x_f$. The colorbars indicate the position in the $x_{f1}$ and $x_{f5}$ coordinate systems, at which the spectra are computed. The subplots represent total variance of the spectra as a function of $x_f$. (b and d) SST map for the areas under consideration.

The breaking criteria and the vertical velocity $w$ across the entire region we observed is shown in Figures 5d and 5h. The line of convergence at the leading edge of the IW packet corresponds to strong downwelling (reaching 0.2 m/s under the assumption of no shear), as shown in Figure 5d. This is followed by a periodic upwelling/downwelling structure for most of the observed wave area. While the given velocities are an estimate, velocities of these magnitude far exceed typical upwelling indices (Bakun, 1973), and are a potent mechanism for vertical transport of the suspended material. The periodic change of ocean color (as shown in Figure 1) is indicative of this process.

Areas of the internal wave undergoing active breaking according to the criteria described above are shown in Figure 5h. The regions where the IW undergo the most energetic breaking is located in the middle section ($y = -2{,}400$ to $-1{,}850$ m), where both the first and second waves are found to be breaking. A closer look at SST imagery at the southern portion shows patches of cold water to the west and the subsequent collapse of the structure closer to the front of the IW packet. This could be due to IW breaking in that region, right before the data collection occurred (which was performed in a south to north direction), that had already dissipated a significant portion of the energy. This hints at the broad range of phenomena that can occur over relatively small spatial scales, motivating the need for more spatial measurements of shoaling and breaking IW.

10.1029/2022GL100622

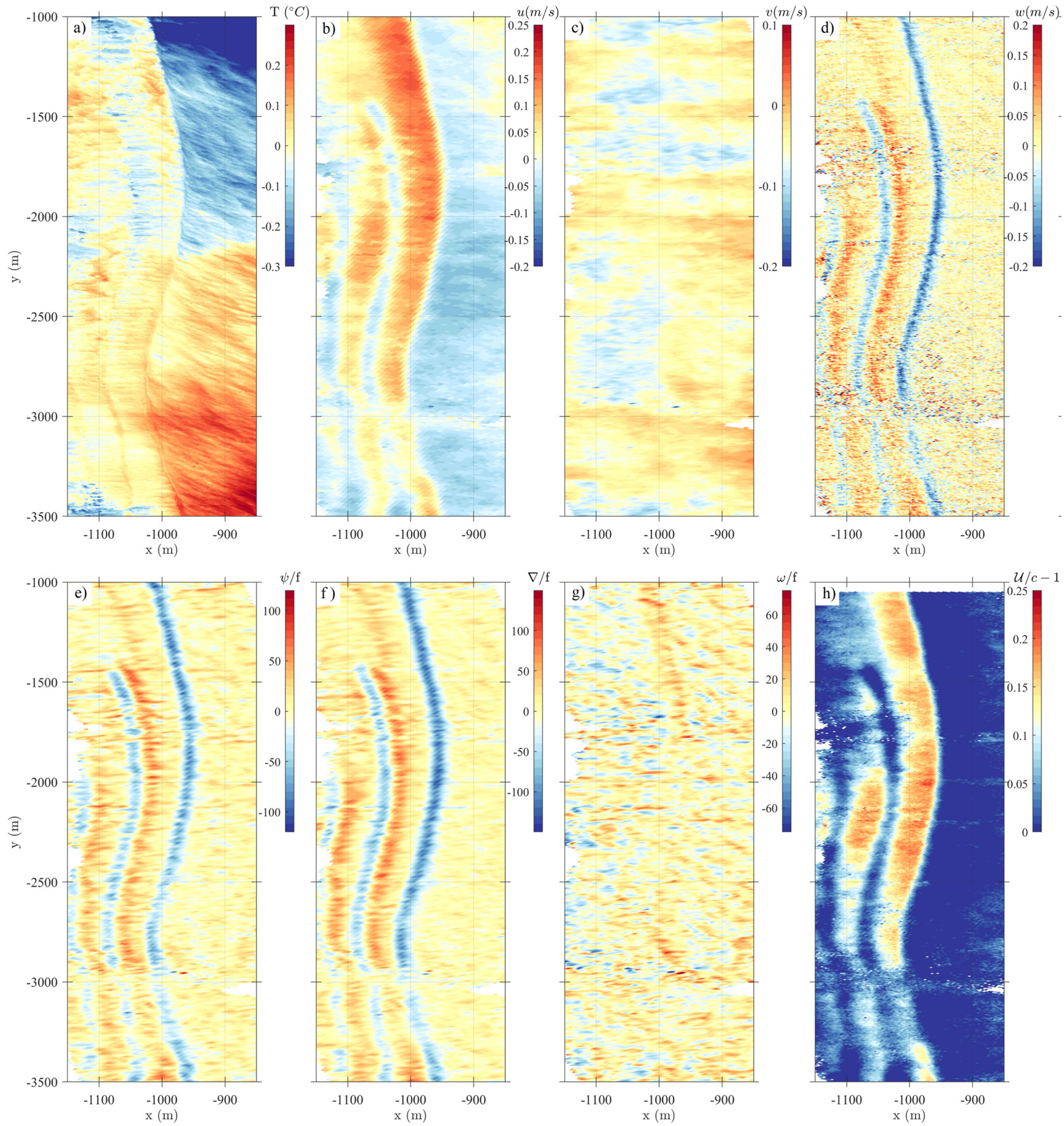


**Figure 5.** (a) SST, surface velocities $u$, $v$ and $w$ (b–d) along with strain rate (e) $\psi = \partial v/\partial x + \partial u/\partial y$, divergence (f) $\nabla = \partial u/\partial x + \partial v/\partial y$, and vorticity (g) $\omega = \partial v/\partial x - \partial u/\partial y$ normalized by the Coriolis frequency $f$. The kinematic wave breaking criteria (h) defined as surface velocity in the direction of wave propagation (minus the ambient current) divided by propagation speed of the internal wave: $\mathcal{U}/c - 1 > 0$. The reference frame here is rotated by 20° in order for $x$ to be aligned with the direction of propagation of the internal wave. Note the patterns of velocity which are mostly consistent along the wave, and strong divergence (reaching more than 100 times that of the Coriolis frequency) along the leading edge of the IW packet.

## 4. Summary

In this paper, we present a unique set of high resolution measurements of the properties of the sea surface as it is being modulated by a very energetic shoaling and breaking internal wave, near Point Sal, CA. We find significant spatial variability in the measured surface thermal structures, from a wave train structure at the center of the observed waves (stretching from the southern tip before collapsing at approximately $y = -1400$ m), to small-scale elongated streaks which appear between individual waves of the IW packet and seem to occur for steepening and breaking IW. Novel and unique spatial observations of surface velocity showed significant modulation in the cross-wave direction, with a strong (over 100$f$) line of convergence at the front of the wave packet. Significant spatial variability of the surface velocity in the along-wave direction was found, associated with different internal wave breaking stages, even though the water depth was approximately uniform over this region. Regions of incipient, ongoing, and recently finished wave breaking were identified, all over a relatively short distance in the along-wave direction (3 km).

Bulk properties of nonlinear IW have been extensively studied and documented (e.g., Colosi et al., 2018; McSweeney, Lerczak, Barth, Becherer, Colosi, et al., 2020; Scotti et al., 2006), based on often sparse arrays of in-situ observations or moored instrumentation with limited directional aperture. Here, we find that the properties of IW can change significantly over relatively short alongshore distances, less than a few hundred meters, highlighting the limitations of using in-situ point measurement observations to unravel the complex transport and mixing mechanisms of shoaling and breaking IW on the inner-shelf. This motivates the need for additional observational campaigns, combining traditional in-situ observations with airborne remote sensing from orbital, crewed or uncrewed platforms.

The structures identified here provide a possible route from quasi-two-dimensional linear IW to the fully three dimensional steep and breaking IW. These structures can be generated by steep waves, as the fastest growing eigenfunctions associated with steep internal wave instabilities are not in the along wave direction (Pullin & Grimshaw, 1985), or with flow instabilities that occur during breaking (see the related discussion in the nearshore community by Handler et al., 2012). A more detailed study of these structures will be the source of future work. Regardless of their generation mechanism, these structures impact vertical velocities and hence modulate the distribution of biological and biogeochemical matter and the advection of heat and horizontal momentum in the coastal environment.

## Data Availability Statement

All presented data can be found at the UCSD Library Digital Collection, https://doi.org/10.6075/J06110G9.

**Acknowledgments**
The authors gratefully acknowledge useful comments from John Colosi. The authors are grateful to Aspen Helicopter for providing flight resources. The authors thank Nick Statom for his support during the field experiments and in the analysis of the MASS data. Additionally, we thank Jack McSweeney and an anonymous referee for helpful comments that have led to an improved manuscript. This research was supported by grants from the Physical Oceanography programs at ONR (Grants N00014-17-1-2171, N00014-14-1-0710, and N00014-17-1-3005), and NASA (Grant 80NSSC19K1688).

## References

Alford, M. H. (2001). Internal swell generation: The spatial distribution of energy flux from the wind to mixed layer near-inertial motions. *Journal of Physical Oceanography*, *31*(8), 2359–2368. https://doi.org/10.1175/1520-0485(2001)031<2359:isgtsd>2.0.co;2

Alpers, W. (1985). Theory of radar imaging of internal waves. *Nature*, *314*(6008), 245–247. https://doi.org/10.1038/314245a0

Badiey, M., Wan, L., & Song, A. (2013). Time-varying three-dimensional mapping of internal waves during the shallow water 2006 experiment. In *Proceedings of meetings on acoustics ICA 2013* (Vol. *19*, p. 070021).

Baines, P. G. (1982). On internal tide generation models. Deep Sea Research Part A. *Oceanographic Research Papers*, *29*(3), 307–338. https://doi.org/10.1016/0198-0149(82)90098-x

Bakun, A. (1973). Coastal upwelling indices, west coast of North America (pp. 1946–1971).

Buckley, M. P., & Veron, F. (2017). Airflow measurements at a wavy air–water interface using PIV and LIF. *Experiments in Fluids*, *58*(11), 1–20. https://doi.org/10.1007/s00348-017-2439-2

Celona, S., Merrifield, S. T., de Paolo, T., Kaslan, N., Cook, T., Terrill, E. J., & Colosi, J. A. (2021). Automated detection, classification, and tracking of internal wave signatures using x-band radar in the inner shelf. *Journal of Atmospheric and Oceanic Technology*, *38*(4), 789–803. https://doi.org/10.1175/jtech-d-20-0129.1

Colosi, J. A., Kumar, N., Suanda, S. H., Freismuth, T. M., & MacMahan, J. H. (2018). Statistics of internal tide bores and internal solitary waves observed on the inner continental shelf off point sal, California. *Journal of Physical Oceanography*, *48*(1), 123–143. https://doi.org/10.1175/jpo-d-17-0045.1

Craig, W., Guyenne, P., & Sulem, C. (2012). The surface signature of internal waves. *Journal of Fluid Mechanics*, *710*, 277–303. https://doi.org/10.1017/jfm.2012.364

Drazen, D. A., Melville, W. K., & Lenain, L. (2008). Inertial scaling of dissipation in unsteady breaking waves. *Journal of Fluid Mechanics*, *611*, 307–332. https://doi.org/10.1017/s0022112008002826

Gregg, M. C. (1989). Scaling turbulent dissipation in the thermocline. *Journal of Geophysical Research*, *94*(C7), 9686–9698. https://doi.org/10.1029/jc094ic07p09686

Handler, R. A., Savelyev, I., & Lindsey, M. (2012). Infrared imagery of streak formation in a breaking wave. *Physics of Fluids*, *24*(12), 121701. https://doi.org/10.1063/1.4769459

Haney, S. R., Simpson, A. J., McSweeney, J. M., Waterhouse, A. F., Haller, M. C., Lerczak, J. A., et al. (2021). Lifecycle of a submesoscale front birthed from a nearshore internal bore. *Journal of Physical Oceanography*, *51*(11), 3477–3493. https://doi.org/10.1175/jpo-d-21-0062.1

Helfrich, K. R., & Melville, W. K. (2006). Long nonlinear internal waves. *Annual Review of Fluid Mechanics*, *38*(1), 395–425. https://doi.org/10.1146/annurev.fluid.38.050304.092129

Huang, Z.-C., Hwang, K.-S., Lenain, L., Melville, W. K., & Hwung, H.-H. (2012). Measurements of surface kinematics and temperature in the surf and swash zones using infrared image velocimetry. *Coastal Engineering Proceedings*, *1*(33), 55. https://doi.org/10.9753/icce.v33.currents.55

Jones, N., Ivey, G., Rayson, M., & Kelly, S. (2020). Mixing driven by breaking nonlinear internal waves. *Geophysical Research Letters*, *47*(19), e2020GL089591. https://doi.org/10.1029/2020gl089591

Kumar, N., Lerczak, J. A., Xu, T., Waterhouse, A. F., Thomson, J., Terrill, E. J., et al. (2021). The inner-shelf dynamics experiment. *Bulletin of the American Meteorological Society*, *102*(5), E1033–E1063. https://doi.org/10.1175/bams-d-19-0281.1

Lamb, K. G. (2014). Internal wave breaking and dissipation mechanisms on the continental slope/shelf. *Annual Review of Fluid Mechanics*, *46*(1), 231–254. https://doi.org/10.1146/annurev-fluid-011212-140701

Lenain, L., & Melville, W. K. (2017). Measurements of the directional spectrum across the equilibrium saturation ranges of wind-generated surface waves. *Journal of Physical Oceanography*, *47*(8), 2123–2138. https://doi.org/10.1175/jpo-d-17-0017.1

Lenain, L., & Pizzo, N. (2021). Modulation of surface gravity waves by internal waves. *Journal of Physical Oceanography*, *51*(9), 2735–2748. https://doi.org/10.1175/jpo-d-20-0302.1

Lucas, A. J., & Pinkel, R. (2022). Observations of coherent transverse wakes in shoaling nonlinear internal waves. *Journal of Physical Oceanography*, *52*(6), 1277–1293. https://doi.org/10.1175/JPO-D-21-0059.1

McSweeney, J. M., Lerczak, J. A., Barth, J. A., Becherer, J., Colosi, J. A., MacKinnon, J. A., et al. (2020). Observations of shoaling nonlinear internal bores across the central California inner shelf. *Journal of Physical Oceanography*, *50*(1), 111–132. https://doi.org/10.1175/jpo-d-19-0125.1

McSweeney, J. M., Lerczak, J. A., Barth, J. A., Becherer, J., MacKinnon, J. A., Waterhouse, A. F., et al. (2020). Alongshore variability of shoaling internal bores on the inner shelf. *Journal of Physical Oceanography*, *50*(10), 2965–2981. https://doi.org/10.1175/jpo-d-20-0090.1

Melville, W. K., Lenain, L., Cayan, D. R., Kahru, M., Kleissl, J. P., Linden, P., & Statom, N. M. (2016). The modular aerial sensing system. *Journal of Atmospheric and Oceanic Technology*, *33*(6), 1169–1184. https://doi.org/10.1175/jtech-d-15-0067.1

Moum, J., Caldwell, D., Nash, J., & Gunderson, G. (2002). Observations of boundary mixing over the continental slope. *Journal of Physical Oceanography*, *32*(7), 2113–2130. https://doi.org/10.1175/1520-0485(2002)032<2113:oobmot>2.0.co;2

Moum, J., Farmer, D., Shroyer, E., Smyth, W., & Armi, L. (2007). Dissipative losses in nonlinear internal waves propagating across the continental shelf. *Journal of Physical Oceanography*, *37*(7), 1989–1995. https://doi.org/10.1175/jpo3091.1

Orlanski, I., & Bryan, K. (1969). Formation of the thermocline step structure by large-amplitude internal gravity waves. *Journal of Geophysical Research*, *74*(28), 6975–6983. https://doi.org/10.1029/jc074i028p06975

Pullin, D., & Grimshaw, R. (1985). Stability of finite-amplitude interfacial waves. Part 2. Numerical results. *Journal of Fluid Mechanics*, *160*, 317–336. https://doi.org/10.1017/s0022112085003500

Romeiser, R., & Graber, H. C. (2015). Advanced remote sensing of internal waves by spaceborne along-track insar—A demonstration with terrasar-x. *IEEE Transactions on Geoscience and Remote Sensing*, *53*(12), 6735–6751. https://doi.org/10.1109/tgrs.2015.2447547

Sandstrom, H., & Elliott, J. (1984). Internal tide and solitons on the Scotian shelf: A nutrient pump at work. *Journal of Geophysical Research*, *89*(C4), 6415–6426. https://doi.org/10.1029/jc089ic04p06415

Scotti, A., Beardsley, R., & Butman, B. (2006). On the interpretation of energy and energy fluxes of nonlinear internal waves: An example from Massachusetts bay. *Journal of Fluid Mechanics*, *561*, 103–112. https://doi.org/10.1017/s0022112006000991

Shroyer, E., Moum, J., & Nash, J. (2010). Energy transformations and dissipation of nonlinear internal waves over New Jersey's continental shelf. *Nonlinear Processes in Geophysics*, *17*(4), 345–360. https://doi.org/10.5194/npg-17-345-2010

Sinnett, G., Ramp, S. R., Yang, Y. J., Chang, M.-H., Jan, S., & Davis, K. A. (2022). Large amplitude internal wave transformation into shallow water. *Journal of Physical Oceanography*, *52*(10), 2539–2554. https://doi.org/10.1175/JPO-D-21-0273.1

Thomas, J., Lerczak, J., & Moum, J. (2016). Horizontal variability of high-frequency nonlinear internal waves in Massachusetts bay detected by an array of seafloor pressure sensors. *Journal of Geophysical Research: Oceans*, *121*(8), 5587–5607. https://doi.org/10.1002/2016jc011866

Thomas, M., Misra, S., Kambhamettu, C., & Kirby, J. T. (2005). A robust motion estimation algorithm for PIV. *Measurement Science and Technology*, *16*(3), 865–877. https://doi.org/10.1088/0957-0233/16/3/031

Venayagamoorthy, S. K., & Fringer, O. (2006). Numerical simulations of the interaction of internal waves with a shelf break. *Physics of Fluids*, *18*(7), 076603. https://doi.org/10.1063/1.2221863

Venayagamoorthy, S. K., & Fringer, O. B. (2007). On the formation and propagation of nonlinear internal boluses across a shelf break. *Journal of Fluid Mechanics*, *577*, 137–159. https://doi.org/10.1017/s0022112007004624

Vlasenko, V., & Stashchuk, N. (2007). Three-dimensional shoaling of large-amplitude internal waves. *Journal of Geophysical Research*, *112*(C11), C11018. https://doi.org/10.1029/2007jc004107

Woods, J. (1968). Wave-induced shear instability in the summer thermocline. *Journal of Fluid Mechanics*, *32*(4), 791–800. https://doi.org/10.1017/s0022112068001035